Polymer Testing 91 (2020) 106834

Contents lists available at ScienceDirect

Polymer Testing

journal homepage: http://www.elsevier.com/locate/polytest

A technique for *in situ* X-ray computed tomography of deformation-induced cavitation in thermoplastics

Sindre Nordmark Olufsen [a,*], Kim Robert Tekseth [b], Dag Werner Breiby [b], Arild Holm Clausen [a], Odd Sture Hopperstad [a]

[a] Centre for Advanced Structural Analysis (CASA), Department of Structural Engineering, NTNU, Norwegian University of Science and Technology, NO-7491, Trondheim, Norway

[b] PoreLab, Department of Physics, NTNU, Norwegian University of Science and Technology, NO-7491, Trondheim, Norway

ARTICLE INFO

Keywords:
In situ X-ray computed tomography
Cavitation
Thermoplastics
Digital image correlation

ABSTRACT

Deformation-induced cavitation influences the mechanical response of polymeric materials, but acquiring *in situ* measurements of the spatial evolution of cavities has typically necessitated the use of synchrotron radiation sources. The objective of this study is to develop and demonstrate a method allowing for *in situ* measurements of deformation-induced cavitation in axisymmetric polymer specimens, using a home-laboratory X-ray computed tomography setup. The method is demonstrated by assessing deformation-induced cavitation of mineral-filled PVC in a repeated loading-unloading experiment. A temporal resolution of about 3 s is obtained by exploiting the axisymmetry of notched round tensile specimens. The evolution of relative density was captured throughout the experiment, revealing an interplay between void nucleation and void growth. Combined with surface deformation measurements obtained by digital image correlation, the present technique yields data suitable for calibration and validation of material models.

1. Introduction

In the pursuit of more sustainable, material-efficient and robust component designs, a detailed understanding of the behaviour of materials under complex loading conditions is needed. When thermoplastic materials are deformed, voids may form by particle decohesion or cavitation of the material [3,16,17,20,24,25,27]. The presence of voids within the material influences several characteristics of the polymer, such as electrical conductivity, optical properties, stress-strain behaviour, pressure sensitivity and ductility. Since the voids may be inhomogeneously distributed within the material and typically have dimensions in the order of a few microns or less, it is challenging to quantify the void volume fraction and the evolution of the voids during a mechanical test. Different techniques have been used to perform *in situ* studies on deformation-induced cavitation in the past, but they typically rely on synchrotron radiation sources [3,27], limiting the availability of such measurements. In order to allow the industry to account for deformation-induced cavitation in the design of structural components, a practical and readily available *in situ* measuring technique, based on a home-laboratory X-ray source rather than a synchrotron, is needed.

The mechanisms governing void formation vary between materials, depending on intrinsic properties, such as microstructure and constituents, as well as external factors, such as stress state [20,24], temperature [15] and rate of deformation [15]. In particular, the stress triaxiality ratio has been observed to have a pronounced influence on cavitation of ductile materials. In semi-crystalline polymers, voids typically form inside the amorphous regions of spherulites [26], whereas craze-like structures are commonly seen in amorphous polymers [10]. Filler particles are commonly used additives in thermoplastics, and can promote cavitation by particle decohesion [19] or cavitation within the particle itself [30].

We can gain understanding about how the stress state influences the formation and growth of voids by subjecting a material sample to a known stress state and determining the morphology and distribution of the voids within the sample after deformation. Notched round tensile specimens are commonly used for this purpose, as the initial stress triaxiality ratio can be tailored by selecting the curvature of the notch. During deformation, however, the geometry and hence the stress state within the notch region will change.

In addition to the stress state, the strain history may influence the

* Corresponding author.
E-mail address: sindre.n.olufsen@ntnu.no (S.N. Olufsen).

https://doi.org/10.1016/j.polymertesting.2020.106834
Received 16 June 2020; Received in revised form 24 August 2020; Accepted 26 August 2020
Available online 11 September 2020

cavitation process. The deformation field within the specimen can in some cases be measured from a series of tomograms by tracking markers [11] or by using digital volume correlation (DVC) [4]. However, this technique relies on the presence of high-contrast internal structures within the specimen, not being present in all materials. Surface-based deformation measurement techniques such as 3D- and 2D-digital image correlation (3D- and 2D-DIC) are practical in industrially relevant experimental setups, but these techniques are limited to measuring the deformation of the outer surface of the specimen. Inverse modelling by finite element analysis is frequently used for determining the internal stress and strain state of a specimen, but is often time consuming and also susceptible to modelling errors.

When voids are present in a tensile specimen at a certain deformation stage, numerous techniques can be applied to quantify the void volume fraction, the morphology and spatial distribution of the voids. A practical approach is to determine the average void volume fraction within a cross-section of the specimen based on its external geometry [1,28]. The drawback of this method is that it relies on assumptions on the kinematics of the specimen, which may be violated when pronounced cavitation is present [16]. Fractography of failed specimens using optical light microscopy (OLM) or scanning electron microscopy (SEM) allows for measurement of the morphology and distribution of dimples on the fracture surface [18], but does not yield insight into the void evolution and the spatial distribution of voids inside the bulk of the material.

If the void morphology inside a specimen is of primary interest, non-destructive *in-situ* characterisation can be done using for example small-angle X-ray scattering (SAXS) [14], which gives volume-averaged signals. However, the spatial distribution of the voids is not obtained from this method. Imaging of the individual voids and their spatial distribution is possible when using techniques such as ptychography [2,6] and X-ray computed tomography (XCT) [3,16,27]. XCT is a particularly attractive method for investigating deformation-induced cavitation. It allows for large regions (cm^3 to dm^3) within the specimen to be imaged and resolution in the micrometer range to be obtained. Home-laboratory XCT is readily available, but the low brilliance of such X-ray sources normally limits studies of void growth in polymers to *ex situ* studies [3,24], considering samples that have been strained to a certain deformation stage before scanning.

Another challenge with home-laboratory XCT is that to achieve a sufficient flux, essentially the full polychromatic spectrum of the X-ray tube source is used, which introduces beam hardening artefacts, typically appearing as a spurious density gradient or streaks within the tomogram. Beam hardening artefacts can be reduced by using relatively high-energy X-rays combined with removal of the low energy part of the spectrum using filtering, or they can be corrected for either in the reconstruction of the tomogram or in the post-processing [13].

Due to the viscous behaviour of most thermoplastics at room temperature, the strain field and the void morphology may change substantially before and during the scanning process, motivating *in situ* measurements. However, performing *in situ* XCT of a tensile specimen during deformation is a challenging task because acquisition times in the order of seconds are needed for each tomogram. Short acquisition times can be obtained by using high brilliance X-ray sources such as synchrotrons [3,27] or by limiting the number of projections acquired for each tomogram.

When a limited number of projections are available for the reconstruction of a tomogram, sophisticated reconstruction techniques are needed to avoid introducing artefacts [5]. However, there are cases where the nature of the investigated specimen (e.g. spatial symmetry, affine transformations, or few sample components allowing for discrete tomography) can be exploited to reduce the number of projections necessary for reconstruction of a tomogram. If the tomogram is axisymmetric, a single projection is sufficient to reconstruct the tomogram, significantly reducing the experimental and computational cost. This approach has allowed for studies of densification of projectiles upon impact [8] and tomography of flames [12]. From a general point of view, tomographic reconstruction is an ill-posed problem where noise in the input data is amplified in the tomogram. The noise level of the tomogram can be improved by making the inverse problem less ill-posed using techniques such as regularization in the reconstruction algorithm, or by preprocessing the input data by frame averaging or filtering [13].

The objective of this study is to demonstrate and verify a procedure for *in situ* measurements of deformation-induced cavitation in axisymmetric polymer specimens using a home-laboratory polychromatic X-ray absorption tomography (XCT) setup. The technique is used here to investigate how the relative density evolves in a mineral-filled PVC during a repeated loading-unloading experiment, which is not feasible using a staggered approach. This study also extends previous work on the same material [19–21,24,25] by including *in situ* field measurements of cavitation synchronised with DIC measurements of surface deformation as well as the true stress-strain behaviour of the material. We reduce the acquisition time of a tomogram by exploiting the axisymmetry of the notched round tensile specimens. Due to the conical beam geometry of the XCT setup, we use an adapted Feldkamp-David-Kress (FDK) reconstruction algorithm [7] similar to the one used by He et al. [12]. The implementation of the reconstruction algorithm can be found in the Python™ package AXITOM [22].

We restrict the XCT part of the study as follows: (i) the density field of the tensile specimen has to be axisymmetric during all states of deformation, (ii) the spatial density distribution and the geometry of the specimen are the metrics of interest, and (iii) the spatial density distribution has to be smooth within the specimen. The relative density is measured by exploiting the proportionality between the density and the X-ray attenuation. Using this approach, individual voids are not resolved and only phenomena changing the relative density are captured. To reduce the noise level in the tomograms, a low pass filter is applied to the radiograms before reconstruction. This approach exploits the smoothness of the relative density fields, but selecting the appropriate filter settings calls for separate experiments. The use of a single projection and a voxel size being large compared to the pore size does not allow the tomograms to be used for DVC. Instead, 2D-DIC based on images captured by a digital camera is used to quantify the deformation of the surface in the notch region of the specimen during deformation. With this approach, the true strain in the notch root can be estimated, individual material points on the surface of the specimen can be tracked, and the diameter reduction can be measured throughout the deformation process. Thus, the true stress-strain curve associated with the *in situ* XCT experiments can be estimated.

The paper is organised as follows. The polymer material and the mechanical testing procedures are presented first, followed by a detailed description of the method developed for *in situ* XCT measurements of axisymmetric tensile specimens. Next, the main test results from the experiment are presented and discussed, and, finally, some concluding remarks are provided. The verification of axisymmetric and calibration of filter settings are compiled in Appendix A and B.

2. Material and mechanical testing

2.1. Material and specimen

To demonstrate the capabilities of the proposed *in situ* XCT measuring technique, deformation-induced cavitation in axisymmetric notched tensile specimens made of mineral-filled PVC was investigated. According to previous experiments on mineral-filled PVC [20,21,24,25], void volume fractions approaching tens of per cent can be reached before failure. Further, SEM investigations have shown that the material contains approx. 24 vol% $CaCO_3$ particles, involving small spherical particles with a typical diameter of 0.2–0.4 μm, and larger irregularly shaped particles [25].

The axisymmetric notched tensile specimens were fabricated using a lathe from 10 mm thick extruded plates provided by Kömmerling

Chemische Fabrik GmbH. The specimen geometry is shown in Fig. 1. The longitudinal axis of the specimen was aligned with the extrusion direction of the plate. A relatively sharp notch radius of 2.0 mm was selected, yielding an initial stress triaxiality ratio of about 0.8 in the centre of the notch [20], and hence the notch promotes void nucleation and growth [20,21,24,25]. The specimen was fixed to the tensile test apparatus by means of threads at both ends. Digital image correlation was facilitated by painting a black speckle pattern on the light grey surface of the specimen using an airbrush.

The cylindrical (r,θ,z) and Cartesian (x,y,z) coordinate systems that will be used in the following are shown in Fig. 2. The z-axes of the coordinate systems are coaxial with the symmetry axis of the specimen. Fig. 2 also shows the coordinate system (a,b) that is applied for the 2000 × 2000 pixel X-ray detector. The origin of the (a,b) system represents the centre of the detector, coinciding with the centre axis of the conical X-ray beam. The horizontal offset between the symmetry axis of the specimen, i.e., the z-axis, and the vertical axis of the detector, i.e., the b-axis, is denoted Δa.

2.2. Experimental setup

The experimental setup is shown in Fig. 3 and consists of four main components, being a) the tensile test apparatus, b) the X-ray CT apparatus, c) the camera used to capture images for the DIC analysis, and d) two light sources. As the specimen is axisymmetric, only projections from a single angle were captured during testing and the tensile test apparatus was therefore not rotated during the test.

A Deben CT5000 tensile test apparatus with a custom-made windowed enclosure was used to perform the tensile tests. This enclosure allows the X-rays to travel through the tensile specimen without interference from the tensile test apparatus as well as providing a free line of sight for the camera used for DIC.

The radiograms were captured by a Nikon XT-225 ST μCT scanner using a tungsten reflection target and a 16 Bit 4 MP PerkinElmer 1620 CN CS detector. An accelerator voltage of 160 kV at a current of 160 μA with 12 dB of amplification was used with an exposure time of 1000 ms. A custom script [9] was used to control the CT scanner, and the frame rate was approx. 0.34 Hz. Beam hardening artefacts were reduced by pre-filtering of the X-rays using a 0.25 mm Cu filter. A source-to-object distance R_{so} = 47.2 mm and a source-to-detector distance R_{sd} = 1125 mm were used, giving a voxel size of 8.4 μm.

Images for 2D-DIC were captured by a 10 Bit 12 MP Basler AC4112-30UM camera using a Samyang f/2.8 ED UMC lens with a focal length of 100 mm at an aperture of F/12. Additional lighting was provided by two LED lights located on both sides of the lens, allowing for a frame rate of 5 Hz.

2.3. Loading procedure

In the *in-situ* experiment, the specimen was continuously deformed according to the displacement program shown in Fig. 4. The displacement program was chosen such that the specimen was elongated in steps with intermediate unloading, allowing for the whole stress-strain curve of the material to be assessed and the unloading response to be investigated. A deformation rate of 1.0 mm/min was used in all steps of the experiment. The force was monitored by a 5 kN load cell at a sample rate of 2.0 Hz.

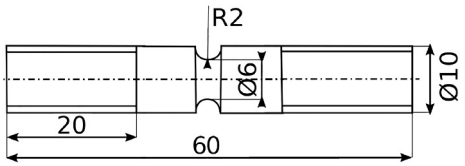

Fig. 1. Axisymmetric notched tensile specimen. All dimensions are in mm.

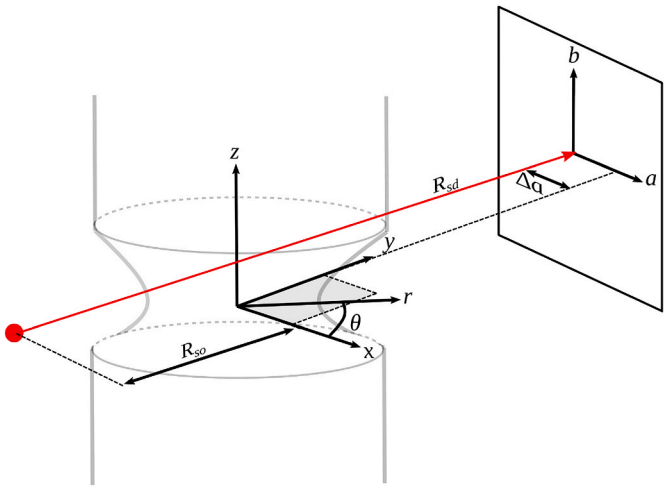

Fig. 2. Coordinate systems of the specimen and the X-ray detector. The position of the X-ray source is indicated by a red dot, and R_{so} and R_{sd} denote the source-to-object distance and the source-to-detector distance, respectively. The horizontal offset between the z-axis of the specimen and the b-axis of the X-ray beam is denoted Δa.

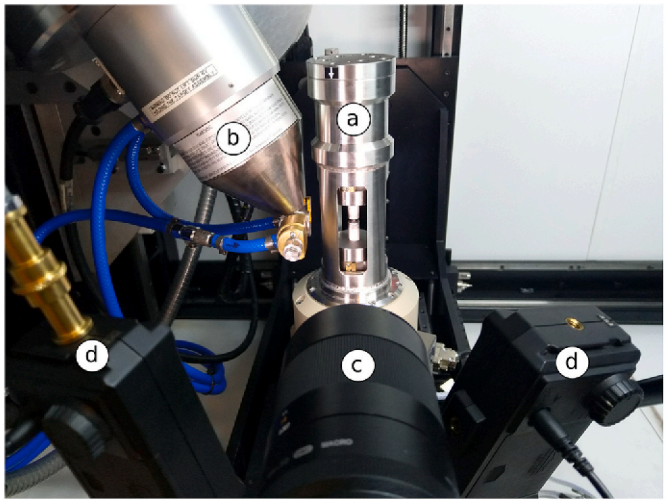

Fig. 3. Experimental setup showing a) tensile test apparatus with specimen, b) X-ray source, c) camera for DIC, and d) light sources.

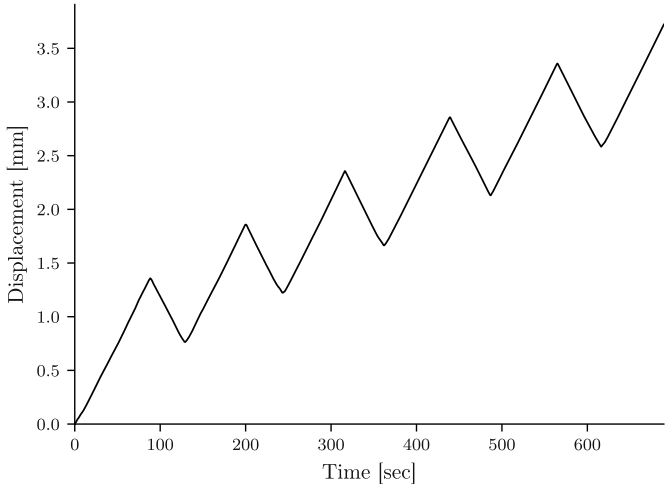

Fig. 4. The programmed displacement applied to deform the specimen.

2.4. Measurement of stress and strain

The average true stress σ and the average true (logarithmic) strain ε_l in the longitudinal direction of the specimen are calculated from the force readings of the tensile apparatus and the strain field in the notch root measured by DIC. It should here be noted that although the cross-sectional area is available from the XCT measurements, the strain measurements obtained by DIC are preferred due to superior accuracy. The 2D-DIC analysis was performed by the open source DIC toolkit μDIC [23], employing B-spline elements with cubic polynomials. The mesh was continuously refined until no further increase in strain was obtained, giving an element size of 45 × 45 pixels. It should be emphasised that 2D-DIC only allows determining strains in the plane orthogonal to the optical axis of the camera. The average true stress is calculated as

$$\sigma = \frac{F}{A} = \frac{F}{A_0 \lambda_r^2} \tag{1}$$

where F is the force measured by the tensile apparatus, A and A_0 are the current and initial area of the minimum cross-section of the notch, respectively, and λ_r is the average radial stretch along the visible circumference at the minimum cross-section. It should here be emphasised that the stress definition does not account for a reduced load-carrying cross-section due to the presence of voids. The average true strain is calculated by

$$\varepsilon_l = \ln(\lambda_l) \tag{2}$$

where λ_l is the average value of the longitudinal stretch along the visible circumference at the minimum cross-section. Olufsen et al. [25] provide a detailed description of how the stretch and strain components are determined from the DIC measurements.

To aid the interpretation of the tomograms and provide data suitable for inverse modelling using finite element analysis, the coordinates of material points laying along $y = 0$ on the notch surface are tracked. The point tracking is extended to 3D by combining the z-coordinates of the material points located along the projected centre axis of the specimen as measured by 2D-DIC and the corresponding r-coordinates from the tomograms. The coordinates were mapped from the DIC analysis to the tomogram by using the notch shoulders as reference points.

3. *In situ* X-ray computed tomography measurements

3.1. Overview

The procedure used to measure dilation caused by deformation-induced cavitation is illustrated in Fig. 5 and contains two main steps divided into five sub-steps.

The purpose of the first main step is to verify the axisymmetry of the notched specimen and to provide a basis for filter calibration. Tomograms using a full set of projections are acquired for two specimens, being an un-deformed specimen and a deformed specimen. The tomograms are used to verify the axisymmetry of the two specimens, and the radiograms are used to determine the appropriate low-pass filter settings that will be used for reconstruction of the axisymmetric tomograms based on projections captured in the subsequent *in situ* experiment. The details of the procedure and results are presented in Appendix A and B. In the second main step of Fig. 5, the *in situ* experiment is performed using a virgin specimen, giving a series of radiograms. Finally, the axisymmetric tomograms are reconstructed.

In the following, all radiograms $\tilde{p}(a,b)$ captured by the X-ray detector have been corrected using a two-point flat field correction given by

$$p(a,b) = \frac{\tilde{p}(a,b) - p_0(a,b)}{\bar{p}(a,b) - p_0(a,b)} \tag{3}$$

where $p_0(a,b)$ and $\bar{p}(a,b)$ are the dark current (no beam) and white (no sample) images, respectively. Frame averaging of 128 exposures was used to obtain the dark current and white images with reduced noise level. The flat field corrected radiograms $p(a,b)$ are henceforth referred to as radiograms.

3.2. Reconstruction of axisymmetric tomograms

The radiograms obtained from the *in situ* experiments are used to reconstruct the axisymmetric tomograms $h(r,z)$. Prior to the reconstruction, the radiograms $p(a,b)$ were filtered using the settings discussed in Appendix B, giving a set of filtered radiograms $p_f(a,b)$. Moreover, the offset Δa between the vertical axis of the detector and the axis of symmetry of the tensile specimen, see Fig. 2, was determined based on the geometric centre of the specimen.

An adapted Feldkamp-David-Kress (FDK) algorithm [7] was employed to reconstruct $h(r,z)$ based on a single low-pass-filtered projection $p_f(a,b)$. The notation used in the following has been adopted from Turbell [31]. The FDK algorithm is modified [22] by assuming that the projections are equal for all rotation angles θ, and by only reconstructing a single plane at $y = 0$ being co-planar with the rz-plane, giving

$$h(r,z) = \int_0^{2\pi} \frac{R_{so}^2}{U(r,\theta)^2} p^F(a(r,\theta), b(r,z,\theta)) d\theta \tag{4}$$

where R_{so} is the distance from the X-ray source to the axis of rotation in pixels, a and b are the pixel coordinates, and the distance $U(r,\theta)$ is given as

$$U(r,\theta) = R_{so} + r\sin\theta \tag{5}$$

The weighted and ramp-filtered projection[1] is defined as

$$p^F(a,b) = \left(\frac{-R_{sd}}{\sqrt{R_{sd}^2 + a^2 + b^2}} \ln\left(p_f(a,b)\right) \right) * g^P(a) \tag{6}$$

where $g^P(a)$ is the ramp-filter kernel, and the arguments of $p^F(a,b)$ are given by

$$a(r,\theta) = R_{sd} \frac{r\cos\theta + \Delta a}{R_{so} + r\sin\theta} \tag{7}$$

and

$$b(r,z,\theta) = z \frac{R_{sd}}{R_{so} + r\sin\theta} \tag{8}$$

where R_{sd} is the source-to-detector distance in pixels. The implementation of the algorithm used in this study is available in the Python™ package AXITOM [22].

4. Results and discussion

Applying the procedure outlined in Appendix A, the undeformed and deformed specimens were concluded to be axisymmetric within the accuracy of the experimental method. Complementary results and discussion with respect to verification of axisymmetry and calibration of filter settings are found in Appendix A and B, respectively.

During the *in situ* experiment, a total of 224 tomograms were captured. The tomograms were synchronised with force, elongation and local strain measurements. The force vs time and force vs displacement curves are shown in Fig. 6. The markers in Fig. 6 signify different characteristic stages of the experiment where (a) represents the undeformed state of the specimen, (b) is at peak force, and (c-l) correspond

[1] Note that the logarithm of the grey scale values of the projection p_f is taken and multiplied by −1, in order to rewrite Beer Lambert's law into line integrals.

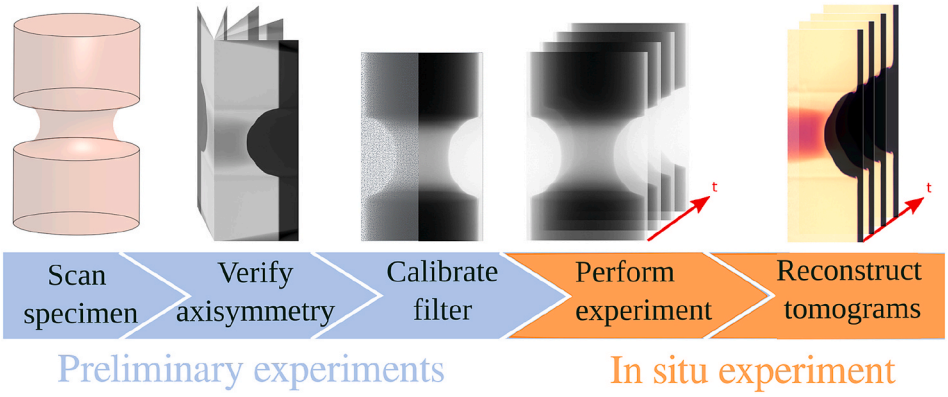

Fig. 5. The experimental procedure divided into two main steps and five sub-steps.

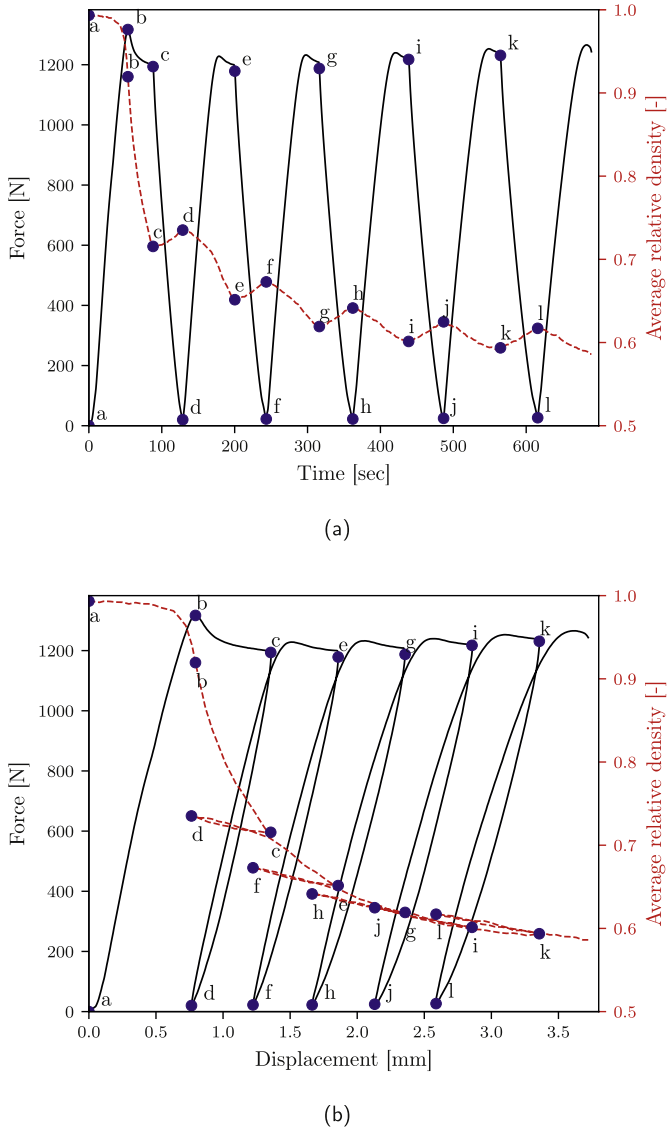

Fig. 6. The force vs time curve is shown in a) and the force vs displacement curve is shown in b). The average relative density is indicated with dashed red lines. The blue dots mark the tomograms shown in Fig. 8.

either to the onset of unloading or to the fully unloaded state.

From Fig. 6 we see that the material initially exhibited a quasi-linear response up to peak force followed by a continuous reduction of the force between (b) and (c). The specimen was then unloaded and reloaded according to the displacement program shown in Fig. 4. The increase in elongation between point (c-e), (e-g), (g-i) and (i-k) is 0.5 mm, see Fig. 4. Fig. 6 b) shows pronounced hysteresis during the unloading-reloading sequence, suggesting that the material exhibits a strain-rate dependent response, conforming to previous findings [24,25].

The average relative density in a slice through the minimum cross-section of the notch was calculated using the procedure described by Olufsen et al. [24], and the results are included in Fig. 6. An abrupt decrease of the density is observed just before peak force, indicating that particle decohesion and void growth are initiated at this stage. Ognedal et al. [19] suggested that softening in mineral-filled PVC could be attributed to particle decohesion at the onset of yielding, being supported by the findings of this study. As the specimen is elongated beyond peak force, the average relative density is reduced from 0.9 to 0.7 before the first unloading is initiated. After this stage, the average relative density does not decrease as rapidly, suggesting that either the nucleation rate decreases for increasing deformation or that the void growth stabilises. During unloading, the average relative density in Fig. 6 b) increases, indicating that there is an elastic contribution to the void volume fraction. When the load is re-applied after unloading, the average relative density decreases without any apparent hysteresis, indicating that the visco-elastic contribution to the void evolution is limited. After the load is re-applied, the average relative density continues to decrease for increasing elongation.

The true stress vs true strain curve is shown in Fig. 7, showing an

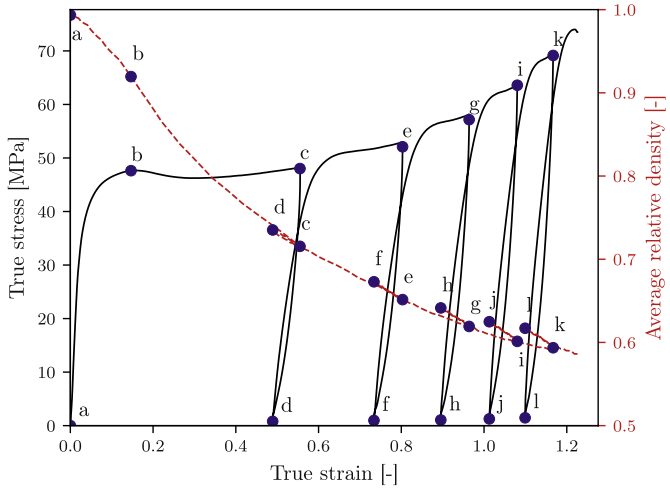

Fig. 7. True stress vs true strain (black line) and average relative density vs true strain (dashed red line) curves. The blue dots mark the tomograms shown in Fig. 8.

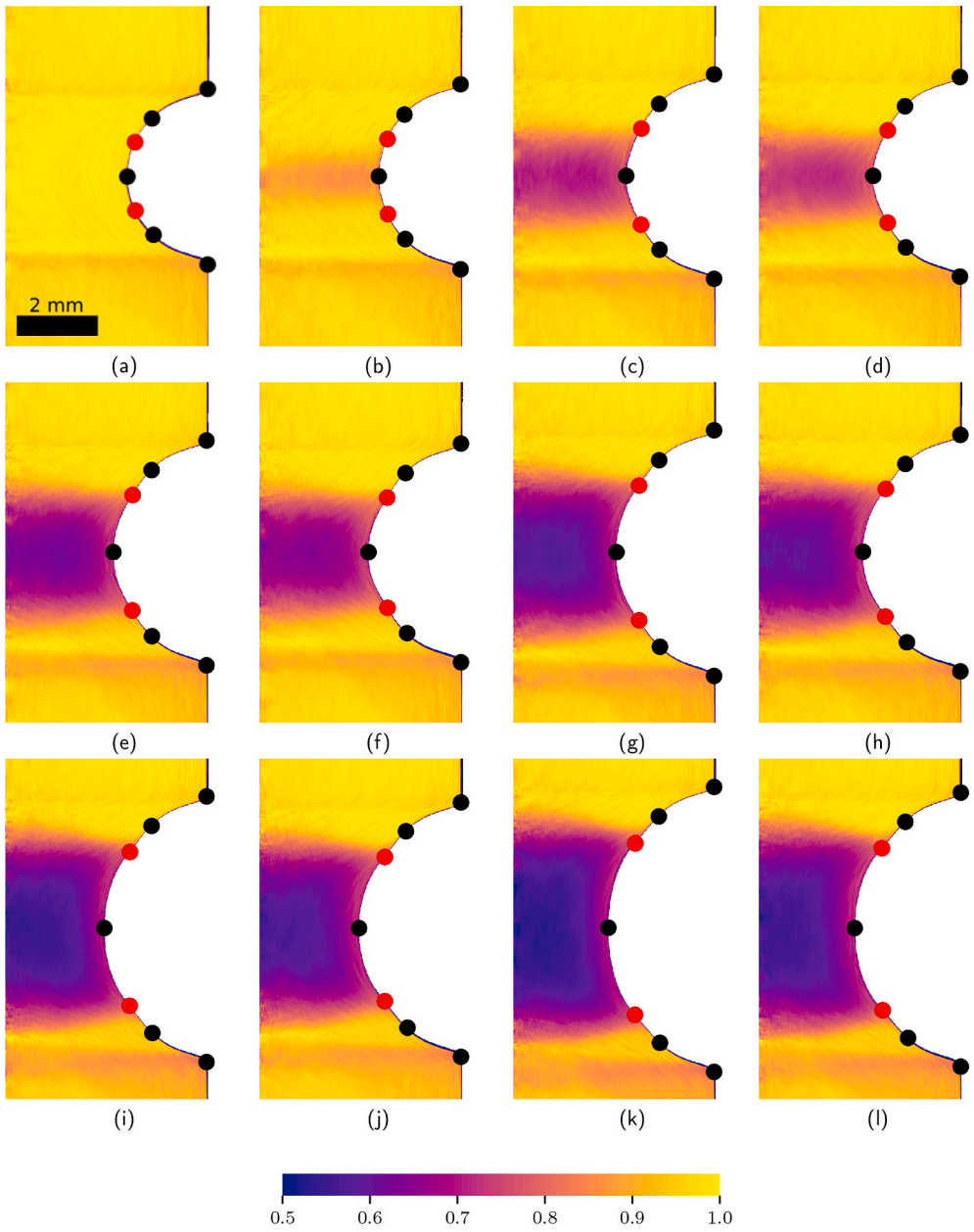

Fig. 8. Relative density fields in the *rz*-plane of the tomograms at the different stages marked in Fig. 6. The dots mark individual material points tracked by 2D-DIC.

increasing hardening rate for increasing true strain. It is interesting to note the large increase in true strain between stage (b) and (c), which is caused by strain localisation. Strain localisation could also appear as softening in the force vs displacement curve by reducing the cross-sectional area. However, softening is still observed in the first part of the true stress vs true strain curve in Fig. 7, supporting void nucleation as the probable softening mechanism. The increment in true strain between the tomograms (c,e,g,i,k) is gradually reduced for large elongations, indicating the presence of cold drawing.

A series of twelve tomograms representing the different stages (a-l) of the experiment is shown in Fig. 8. To ease the interpretation of the results, seven material points tracked by 2D-DIC are marked on the notch surface in Fig. 8.

The relative density evolution displayed in Fig. 6 shows that pronounced dilation initiates at the elongation corresponding to peak force. In Fig. 8b), a radial band with a relative density in the order of 0.9 has formed, and the relative density decreases rapidly for further elongation. At this stage, a neck has formed within the notched section of the specimen, changing the notch root radius [25]. An interesting observation is that for deformations beyond stage (c), the band with reduced density is confined between two material points on the notch surface identified with red markers in Fig. 8, and appears not to spread into new material for increasing deformation. This observation suggests that particle-matrix decohesion happens up to stage (c) but to a much lesser extent beyond this point.

It appears from Fig. 8 that the relative density varies within the notch, being higher close to the surface than in the interior. To get a closer view of this, the relative density distribution along the radial axis at the minimum cross-section of the notch is shown for tomogram (a,b,c, e,g,i,k) in Fig. 9. As the specimen is elongated, the radial density distribution changes from being uniform (a-c) towards a parabolic shape (e-k), suggesting that the governing parameters for void growth are both the plastic strain, which initially is largest on the specimen surface, and the stress triaxiality ratio, which is larger in the interior of the specimen [20].

The frame rate used in this experiment represents a conservative

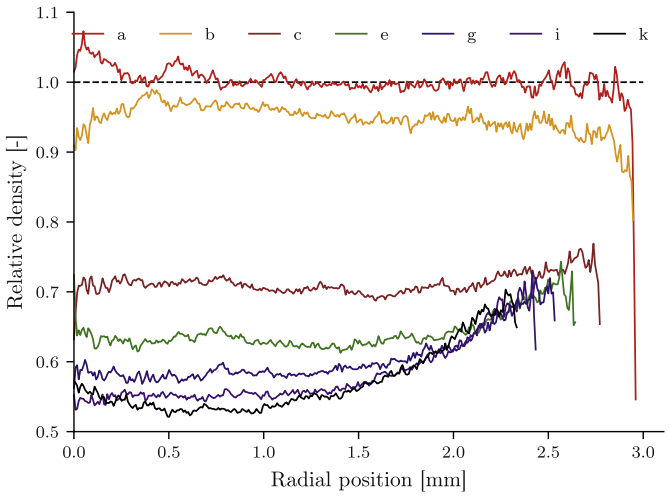

Fig. 9. Radial relative density distribution for tomogram (a,b,c,e,g,i,k) shown in Fig. 8.

setting that can be further optimized. A script was used to control the CT apparatus but at the cost of saving the images to a disk between each acquisition, thus reducing the frame rate. Motion blur is a concern when long exposure times are used for a continuously deformed specimen, but there is no visible evidence of blurring of the edges in the radiograms captured herein.

The offset of the symmetry axis Δa was found for every frame, varying between 36 and 31 pixels during the whole deformation procedure. The out-of-plane position of the symmetry axis is not known and an offset of the symmetry axis in the y-direction would yield a slightly different magnification as well as an error related to the weighting of the radiogram pixels in the reconstruction. However, assuming that this offset in the y-direction is in the same order of magnitude as Δa, this error will have limited influence on the results.

5. Concluding remarks

We have demonstrated an experimental procedure allowing for *in situ* measurements of deformation-induced cavitation in mineral-filled PVC using a home-laboratory X-ray setup. The specimen was subjected to a repeated loading-unloading sequence, exemplifying how this technique facilitates capturing transient phenomena. By exploiting the axisymmetry of the tensile specimen, the acquisition time for a tomogram was reduced by several orders of magnitude compared to full scans. As no rotation of the tensile specimen is necessary during the experiment, combination with other measuring techniques such as digital image correlation is facilitated. The proposed procedure makes *in situ* measurements of material cavitation available to a broader audience and opens up for exciting possibilities for material model development, calibration and validation.

Declaration of competing interest

The authors declare that they have no known competing financial interests or personal relationships that could have appeared to influence the work reported in this paper.

Acknowledgements

The authors gratefully appreciate the financial support from the Research Council of Norway through the Centre for Advanced Structural Analysis, Project No. 237885 (SFI-CASA). The use of the X-ray laboratory at the Department of Physics at NTNU, partially financed by the Norwegian Research Council through project no. 208896, is acknowledged. KRT and DWB thank the Research Council of Norway for financial funding through the FRINATEK project 4D-CT, project no. 275182, and the Centre of Excellence funding scheme, project no. 262644 (SFF-PoreLab).

Appendix

A. Verification of axisymmetry

In this sub-step of the analysis, see Fig. 5, the axisymmetry of an undeformed and a deformed specimen is verified by checking that their respective tomograms $f(r,\theta,z)$ fulfil cylinder symmetry. The deformed specimen was elongated to obtain a state with substantial cavitation in the notch region and then stored to relax any residual stresses. Applying the procedure of Olufsen et al. [24], the tomogram is considered to be axisymmetric if all variation along the θ-axis is comparable or smaller than the noise level of the tomogram.

The undeformed and deformed specimens were scanned using the Nikon XT-225 ST μCT apparatus, giving a stack of projections for 3142 angles uniformly spaced within a full revolution. Based on these projections, a tomogram $\tilde{g}(x,y,z)$ was reconstructed using the software Nikon CT-pro. To ease the interpretation of the tomogram, the grey-scale values were normalized to the grey-scale of the background g_0 and to the grey-scale of undeformed material $\bar{g}$. The values of $\bar{g}$ and g_0 were calculated as the average value of a rectangular section covering the region of interest in the tomograms. A relative density field was then obtained by

$$g(x,y,z) = \frac{\tilde{g}(x,y,z) - g_0}{\bar{g} - g_0} \tag{9}$$

The relative density field $g(x,y,z)$ was re-sampled into cylindrical coordinates $f(r,\theta,z)$ using a custom script and the software ImageJ [29]. The z-axis of the tomogram was chosen to be coaxial with the symmetry axis of the specimen. The symmetry axis was placed at the geometric centre of the specimen, determined by binarization of the tomogram into object and background by thresholding.

The circumferential average value $\mu_f(r,z)$ of $f(r,\theta,z)$ along the θ-axis was calculated as

$$\mu_f(r,z) = \frac{1}{N_\theta}\sum_{i=1}^{N_\theta} f(r,\theta_i,z) \tag{10}$$

where N_θ is the number of angular increments. The number of angular increments was selected such that a new pixel is sampled at the outer perimeter of the specimen for each angular increment. The circumferential standard deviation $\sigma_f(r,z)$ along the θ-axis is given by

$$\sigma_f(r,z) = \sqrt{\frac{1}{N_\theta}\sum_{i=1}^{N_\theta}\left(f(r,\theta_i,z) - \mu_f(r,z)\right)^2} \tag{11}$$

and the coefficient of variation $C_{vf}(r,z)$ was calculated as

$$C_{vf}(r,z) = \frac{\sigma_f(r,z)}{\mu_f(r,z)} \tag{12}$$

An estimate of the noise level $\Delta\sigma_f$ of the tomogram was determined by calculating the standard deviation of the grey-scale values of a sub-frame $f(r,\theta_i,z)$ covering undeformed material in a single radial slice θ_i.

The circumferential average μ_f, standard deviation σ_f and coefficient of variation C_{vf} are shown in Fig. 10 (a,b,c) for the deformed specimen, and in Fig. 10 (d,e,f) for an undeformed specimen, using 5026 angular increments.

The circumferential average μ_f in Fig. 10a) shows a pronounced decrease in density in the interior of the notch for the deformed specimen. In addition, a narrow band with lower density can be seen at both notch shoulders, and is here interpreted as an artefact, possibly caused by misalignment in the tomography setup. This artefact was reduced in later tests by rounding the notch shoulders.

The undeformed specimen, see Fig. 10d), has a slightly higher relative density of 1.02 in the notch region, also observed in previous studies [24]. The higher density could be caused by scattering artefacts, but due to the relatively low magnitude of this artefact, no further investigations were performed to confirm this. For the undeformed specimen, there are no visible signs of density variations in the radial direction, suggesting that the use of a relatively high accelerator voltage and pre-filtering has reduced the beam hardening artefacts ("cupping") to an acceptable level.

The standard deviation fields σ_f shown in Fig. 10 (b,e) display values in the range between 0.06 and 0.07 in the interior of the specimen. The standard deviation of the grey-scale values within a sub-frame of a single radial slice is 0.07, suggesting that noise is the primary source of variation in the circumferential direction. The coefficient of variation C_{vf} is approx. 0.06 for the undeformed sections of the tomograms in Fig. 10 (c,f). The coefficient of variation C_{vf} increases to approx. 0.1 in the notched section for the deformed specimen, caused by the reduced relative density within the highly deformed section of the notch.

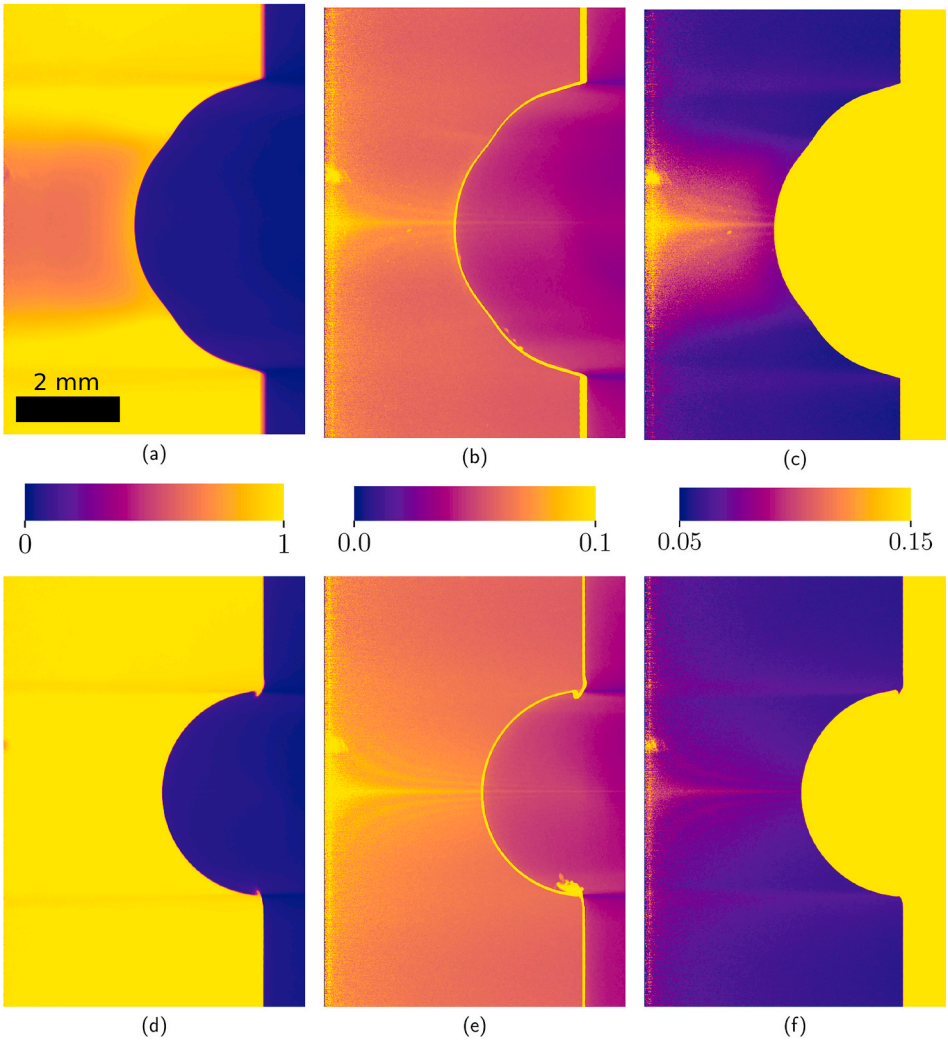

Fig. 10. Results obtained for each step of the procedure used to verify the assumption of axisymmetry for a deformed specimen (a,b,c) and an undeformed specimen (d,e,f). The average value μ_f of the radial planes is shown in subfigure (a,d), standard deviation σ_f of the radial planes is shown in (b,e), and the coefficient of variation C_{vf} in (c,f).

In conclusion: as the noise of the tomograms dominates the variation along the radial axis of the specimen, the specimens can be considered as axisymmetric.

B. Calibration of filter settings

It is recalled from Fig. 5 that another purpose with the full set of projections was to determine the settings of an appropriate filter to be applied to the radiograms before reconstruction of the tomogram $h(r,z)$ in the *in situ* experiment. Such a filter is required to reduce the noise level of the axisymmetric tomogram. In this sub-step, the mean relative density field $\mu_f(r,z)$ is compared with a tomogram $h(r,z)$ which is based on a single filtered projection $p_f(a,b)$. The single projection used to reconstruct $h(r,z)$ was picked randomly from the stack used in the calculation of $\mu_f(r,z)$. In order to identify where the largest deviations between $\mu_f(r,z)$ and $h(r,z)$ occur, the absolute error field $\varepsilon_h(r,z)$ is calculated as

$$\varepsilon_h(r,z) = \left|\mu_f(r,z) - h(r,z)\right| \tag{13}$$

As a metric for the match between $\mu_f(r,z)$ and the tomogram $h(r,z)$ reconstructed from the single filtered projection $p_f(a,b)$, the root-mean-square error (RMSE) is defined by

$$\mathrm{RMSE}(h) = \sqrt{\frac{1}{m}\sum_{j=1}^{m}\left(\mu_f(r_j,z_j) - h(r_j,z_j)\right)^2} \tag{14}$$

where j denotes the pixel with coordinates (r_j,z_j) and m is the number of pixels. The optimal filter settings are here defined as the settings that minimise $\mathrm{RMSE}(h)$.

A median filter and a Gaussian low-pass filter were selected as candidates for pre-filtering of the radiograms before reconstruction. The corresponding error fields $\varepsilon_h(r,z)$ for a median filter window size of 5, 21 and 49 pixels and a Gaussian filter with standard deviation of 2,7 and 19 pixels are shown in Fig. 11. The corresponding RMS error vs filter kernel size is shown in Fig. 12. As the standard deviation of the Gaussian kernel is increased, the RMS error is reduced to a value of 0.0318 for a standard deviation of 6.0 pixels. Note that the magnitude refers to the relative density being normalized between 0 and 1. For a further increase of kernel size, the RMS error increases, because of the blurring of the edges of the specimen as can be seen in Fig. 11 (f). The median filter is edge-preserving and is therefore particularly attractive for this application. By increasing the median kernel size, the RMS error is reduced monotonically, but only minor improvements are observed beyond a kernel size of 21 pixels where an RMS error of 0.0314 is observed. However, the median filter introduces streak-like artefacts. Nevertheless, a median filter with a kernel size of 41 pixels was used for pre-filtering of radiograms before reconstruction of the tomogram.

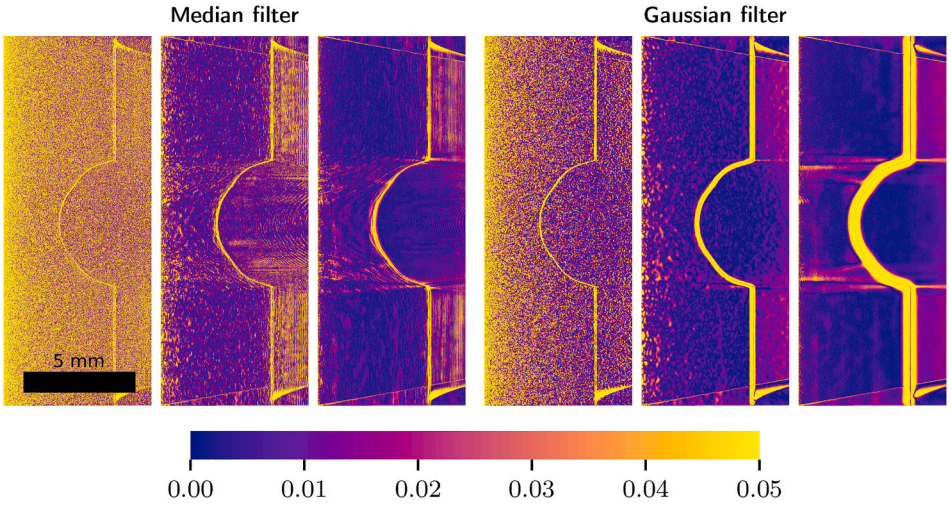

Fig. 11. Absolute error between full and axisymmetric tomograms, ε_h, for a median filter with window size of a) 5, b) 21 and c) 49 pixels. The corresponding fields are shown for a Gaussian low-pass filter with a standard deviation of d) 2, e) 7 and f) 19 pixels.

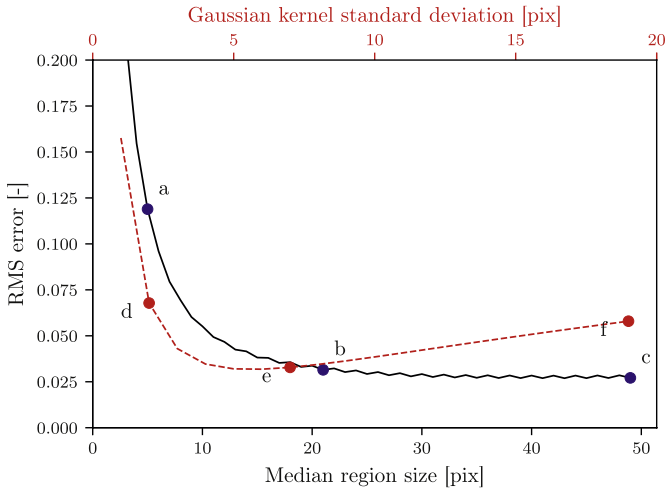

Fig. 12. Root-mean-square error RMSE(h) between a reference tomogram and an axisymmetric tomogram, for different degrees of pre-filtering using a Gaussian low-pass filter (red) and a median filter (black). The error fields shown in Fig. 11 are marked by circular dots.

Spatio-temporal filters have also been considered, but the Eulerian nature of the radiograms complicates the application of such filters. If a low-pass filter is applied along the time axis for each pixel, different material points will occupy this pixel for different time frames, possibly introducing errors. Due to this problem, spatio-temporal filtering was left out of this study.

Data availability statement

The raw/processed data required to reproduce these findings cannot be shared at this time due to technical or time limitations.

References

[1] M. Andersen, O.S. Hopperstad, A.H. Clausen, Volumetric strain measurement of polymeric materials subjected to uniaxial tension, Strain 55 (2019), https://doi.org/10.1111/str.12314. https://onlinelibrary.wiley.com/doi/abs/10.1111/str.12314.

[2] J. Bø Fløystad, E.T.B. Skjønsfjell, M. Guizar-Sicairos, K. Høydalsvik, J. He, J. W. Andreasen, Z. Zhang, D.W. Breiby, Quantitative 3D X-ray imaging of densification, delamination and fracture in a micro-composite under compression, Adv. Eng. Mater. 17 (2015) 545–553, 10.1002/adem.201400443, https://onlinelibrary.wiley.com/doi/abs/10.1002/adem.201400443.

[3] N. Brusselle-Dupend, E. Rosenberg, J. Adrien, Characterization of cavitation development while tensile testing PVF2 using 3D X-ray microtomography, Mater. Sci. Eng. 530 (2011) 36–50, https://doi.org/10.1016/j.msea.2011.09.009, 10.1016/j.msea.2011.09.009.

[4] A. Buljac, C. Jailin, A. Mendoza, J. Neggers, T. Taillandier-Thomas, A. Bouterf, B. Smaniotto, F. Hild, S. Roux, Digital volume correlation: review of progress and challenges, Exp. Mech. 58 (2018) 661–708, 10.1007/s11340-018-0390-7, http://link.springer.com/10.1007/s11340-018-0390-7.

[5] T. Bultreys, M.A. Boone, M.N. Boone, T. De Schryver, B. Masschaele, L. Van Hoorebeke, V. Cnudde, Fast laboratory-based micro-computed tomography for pore-scale research: illustrative experiments and perspectives on the future, Adv. Water Resour. 95 (2016) 341–351, https://doi.org/10.1016/j.advwatres.2015.05.012, 10.1016/j.advwatres.2015.05.012.

[6] M. Esmaeili, J.B. Fløystad, A. Diaz, K. Høydalsvik, M. Guizar-Sicairos, J. W. Andreasen, D.W. Breiby, Ptychographic X-ray tomography of silk fiber hydration, Macromolecules 46 (2013) 434–439, https://doi.org/10.1021/ma3021163.

[7] L.A. Feldkamp, L.C. Davis, J.W. Kress, Practical cone-beam algorithm, J. Opt. Soc. Am. 1 (1984) 612, 10.1364/JOSAA.1.000612, http://josaa.osa.org/abstract.cfm?URI=josaa-1-6-612 https://www.osapublishing.org/abstract.cfm?URI=josaa-1-6-612.

[8] E. Fugelso, Material Density Measurements from Dynamic Flash X-Ray Radiographs Using Axisymmetric Tomography. Technical Report, Los Alamos Publication, 1981.

[9] P. Gajjar, J.S. Jørgensen, J.R.A. Godinho, C.G. Johnson, A. Ramsey, P.J. Withers, New software protocols for enabling laboratory based temporal CT, Rev. Sci. Instrum. 89 (2018), 093702. http://aip.scitation.org/doi/10.1063/1.5044393, 10.1063/1.5044393.

[10] C. G'Sell, J.M. Hiver, A. Dahoun, Experimental characterization of deformation damage in solid polymers under tension, and its interrelation with necking, Int. J. Solid Struct. 39 (2002) 3857–3872, https://doi.org/10.1016/S0020-7683(02)00184-1, 10.1016/S0020-7683(02)00184-1.

[11] K. Haldrup, S.F. Nielsen, J.A. Wert, A general methodology for full-field plastic strain measurements using X-ray absorption tomography and internal markers, Exp. Mech. 48 (2008) 199–211, https://doi.org/10.1007/s11340-007-9079-z.

[12] Y. He, G. Lu, Y. Yan, 3-D reconstruction of an axisymmetric flame based on cone-beam tomographic algorithms, in: Proceedings of the International Conference on Sensing Technology, ICST, 2016, https://doi.org/10.1109/ICSensT.2016.7796314, 0–5.

[13] J. Hsieh, Computed tomography: principles, design, artifacts, and recent advances. SPIE, 10.1117/3.2197756, http://ebooks.spiedigitallibrary.org/book.aspx?, 2015.

[14] S. Humbert, O. Lame, J.M. Chenal, C. Rochas, G. Vigier, New insight on initiation of cavitation in semicrystalline polymers: in-situ SAXS measurements, Macromolecules 43 (2010) 7212–7221, https://doi.org/10.1021/ma101042d.

[15] J. Johnsen, F. Grytten, O.S. Hopperstad, A.H. Clausen, Influence of strain rate and temperature on the mechanical behaviour of rubber-modified polypropylene and cross-linked polyethylene, Mech. Mater. 114 (2017) 40–56, https://doi.org/10.1016/j.mechmat.2017.07.003, 10.1016/j.mechmat.2017.07.003.

[16] L. Laiarinandrasana, O. Klinkova, F. Nguyen, H. Proudhon, T.F. Morgeneyer, W. Ludwig, Three dimensional quantification of anisotropic void evolution in deformed semi-crystalline polyamide 6, Int. J. Plast. 83 (2016) 19–36, https://doi.org/10.1016/j.ijplas.2016.04.001, 10.1016/j.ijplas.2016.04.001.

[17] L. Laiarinandrasana, T.F. Morgeneyer, H. Proudhon, C. Regrain, Damage of semicrystalline polyamide 6 assessed by 3D X-ray tomography: from microstructural evolution to constitutive modeling, J. Polym. Sci. B Polym. Phys. 48 (2010) 1516–1525, https://doi.org/10.1002/polb.22043, 10.1002/polb.22043.

[18] A.S. Ognedal, Large-deformation behaviour of thermoplastics at various stress states, Ph.D. thesis, NTNU, 2012.

[19] A.S. Ognedal, A.H. Clausen, T. Berstad, T. Seelig, O.S. Hopperstad, Void nucleation and growth in mineral-filled PVC - an experimental and numerical study, Int. J. Solid Struct. 51 (2014) 1494–1506, https://doi.org/10.1016/j.ijsolstr.2013.12.042, 10.1016/j.ijsolstr.2013.12.042.

[20] A.S. Ognedal, A.H. Clausen, A. Dahlen, O.S. Hopperstad, Behavior of PVC and HDPE under highly triaxial stress states: an experimental and numerical study, Mech. Mater. 72 (2014) 94–108, https://doi.org/10.1016/j.mechmat.2014.02.002.

[21] A.S. Ognedal, A.H. Clausen, M. Polanco-Loria, A. Benallal, B. Raka, O. S. Hopperstad, Experimental and numerical study on the behaviour of PVC and HDPE in biaxial tension, Mech. Mater. 54 (2012) 18–31, https://doi.org/10.1016/j.mechmat.2012.05.010, 10.1016/j.mechmat.2012.05.010.

[22] S.N. Olufsen, AXITOM: a Python package for reconstruction of axisymmetric tomograms acquired by a conical beam, Journal of Open Source Software 4 (2019) 1704, 10.21105/joss.01704, https://joss.theoj.org/papers/10.21105/joss.01704.

[23] S.N. Olufsen, M.E. Andersen, E. Fagerholt, DIC: an open-source toolkit for digital image correlation, Software 11 (2020), 100391. https://doi.org/10.1016/j.softx.2019.100391. https://linkinghub.elsevier.com/retrieve/pii/S2352711019301967, 10.1016/j.softx.2019.100391.

[24] S.N. Olufsen, A.H. Clausen, D.W. Breiby, O.S. Hopperstad, X-ray computed tomography investigation of dilation of mineral-filled PVC under monotonic loading, Mech. Mater. 142 (2020), 103296. https://doi.org/10.1016/j.mechmat.2019.103296. https://linkinghub.elsevier.com/retrieve/pii/S0167663619305642, 10.1016/j.mechmat.2019.103296.

[25] S.N. Olufsen, A.H. Clausen, O.S. Hopperstad, Influence of stress triaxiality and strain rate on stress-strain behaviour and dilation of mineral-filled PVC, Polym. Test. 75 (2019) 350–357, 10.1016/j.polymertesting.2019.02.018, https://linkinghub.elsevier.com/retrieve/pii/S0142941818318580.

[26] A. Pawlak, A. Galeski, A. Rozanski, Cavitation during deformation of semicrystalline polymers, Prog. Polym. Sci. 39 (2013) 921–958, https://doi.org/10.1016/j.progpolymsci.2013.10.007, 10.1016/j.progpolymsci.2013.10.007.

[27] P.A. Poulet, G. Hochstetter, A. King, H. Proudhon, S. Joannès, L. Laiarinandrasana, Observations by in-situ X-ray synchrotron computed tomography of the microstructural evolution of semi-crystalline Polyamide 11 during deformation, Polym. Test. 56 (2016) 245–260, https://doi.org/10.1016/j.polymertesting.2016.10.023, 10.1016/j.polymertesting.2016.10.023.

[28] M. Rossi, L.C.K. Genovese, A.L.F. Nalli, Evaluation of Volume Deformation from Surface DIC Measurement D, 2018, pp. 1181–1194.

[29] J. Schindelin, I. Arganda-Carreras, E. Frise, V. Kaynig, M. Longair, T. Pietzsch, S. Preibisch, C. Rueden, S. Saalfeld, B. Schmid, J.Y. Tinevez, D.J. White, V. Hartenstein, K. Eliceiri, P. Tomancak, A. Cardona, Fiji: an open-source platform for biological-image analysis, Nat. Methods 9 (2012) 676–682, https://doi.org/10.1038/nmeth.2019.

[30] A.C. Steenbrink, E. Van Der Giessen, P. Wu, Void growth in glassy polymers, J. Mech. Phys. Solid. 45 (1997) 405–437, https://doi.org/10.1016/S0022-5096(96)00093-2, 10.1016/S0022-5096(96)00093-2.

[31] H. Turbell, Cone-beam reconstruction using filtered backprojectionn. Ph.D. Thesis. Linköpings universitet. http://citeseerx.ist.psu.edu/viewdoc/download?doi=10.1.1.134.5224&rep=rep1&type=pdf, 2001.